Semnan University

Progress in Physics of Applied Materials

journal homepage: https://ppam.semnan.ac.ir/

Effect of Sintering Temperature on Phase Characteristic and Grain Size of $La_{0.7}AE_{0.3}MnO_3$ (AE=Ba/Ca/Sr) Ceramics Prepared by Sol-Gel Method

Ratna Isnanita Admi[a], Budhy Kurniawan*[a], Sitti Ahmiatri Saptari[b], Gede Yudharma[a], Dicky Rezky Munazat[a]

[a] *Department of Physics, Universitas Indonesia, Depok, 16424, Indonesia*
[b] *Department of Physics, State Islamic University Syarif Hidayatullah Jakarta, South Tangerang, 15412, Indonesia*

ARTICLE INFO

Article history:
Received: 19 April 2024
Revised: 22 May 2024
Accepted: 25 May 2024

Keywords:
Perovskite
Lanthanum manganite
Sintering temperatur
Grain size
Sol-Gel

ABSTRACT

We investigate the impact of sintering temperature on changes in phase characteristics and grain size in the $La_{0.7}AE_{0.3}MnO_3$ (AE=Ba/Ca/Sr) materials synthesized by the sol-gel method. The materials were sintered at different sintering temperatures of 700°C, 800°C, 900°C, and 1200°C. The refinement of the X-ray Diffraction (XRD) pattern revealed that the $La_{0.7}Ca_{0.3}MnO_3$ and $La_{0.7}Sr_{0.3}MnO_3$ materials exhibited a single phase across all sintering temperatures. For $La_{0.7}Ba_{0.3}MnO_3$, a single-phase structure was observed only at sintering temperature above 800°C. All materials showed an increase in peak intensity and a shift in peak in the range angle 31°-34° towards higher angles correlated to increased sintering temperature. Sintering temperature plays an important role in controlling the grain size. Images obtained by Scanning Electron Microscope (SEM) showed the morphology of $La_{0.7}Sr_{0.3}MnO_3$ sintered at different temperatures (700°C, 800°C, and 900°C). The morphology results show an increment in the average grain size with range of 41.05 – 69.27nm because of the grain growth as the sintering temperature.

1. Introduction

Manganite is an oxide-perovskite family that is the most interesting to study in terms of its special physical properties. The intrinsic properties of *Colossal Magnetoresistance* (CMR) in manganite have been extensively studied. A very large magnetoresistance effect is observed from the close interaction between the transport of magnetic and electric compounds from manganite [1]. Valence doping variations of manganese oxide $R_{1-x}A_xMnO_3$ (R represents rare earth elements such as La^{3+}, Pr^{3+}, Nd^{3+}, etc. A represents alkaline earth metals divalent such as Ba^{2+}, Ca^{2+}, Sr^{2+}, etc.) have attracted increasing interest and are related unique electromagnetism like interactions between spin, charge, and orbitals that depend on the stoichiometry and structure of the material [2-4]. This matter is related to validation draft physiques such as incident double exchange and the associated Jahn-Teller distortion [3], [5-6] amount mixture of different valence Mn^{3+}/Mn^{4+} ions with adjusted doping variation parameters [7]. Manganite is a promising material for various electronic applications, including magnetic reading heads for hard disks, magnetoresistive random access memory (MRAM), and field sensors. Additionally, it has potential uses in magnetic cooling applications [3]. Among the various systems of multifunctional manganite, lanthanum manganite ($La_{1-x}A_xMnO_3$) has been widely studied because of characteristic its richness [8-17].

The magnetic and electrical characteristics of polycrystalline manganite are significantly influenced by microstructural conditions like grain boundaries, size, and porosity. Alterations in sintering time, temperature, and processing route can lead to variations in the microstructure, thereby affecting these properties [7], [18]. In the 21st century, many researchers have been interested in nanoscale materials including manganite.

* Corresponding author.
E-mail address: budhy.kurniawan@sci.ui.ac.id

Cite this article as:
Admi, R.I., Kurniawan, B., Saptari, S.A. Yudharm, G. and Munazat, D.R., 2024. Effect of Sintering Temperature on Phase Characteristic and Grain Size of $La_{0.7}AE_{0.3}MnO_3$ (AE=Ba/Ca/Sr) Ceramics Prepared by Sol-Gel Method. Progress in Physics of Applied Materials, 4(1), pp. 93-101. DOI: 10.22075/PPAM.2024.33788.1096

Nanostructured manganite shows electricity and magnetism behaviors that are different from those of manganese in amount [7]. The sol-gel method is a well-known technique for making nano and microsized manganite of high quality because of the simple process and good control of texture, size, and properties of surface ingredients, ease of application, low cost, high quality, and production material with a large surface area [19].

The significant value of favorable properties like electrical, magnetic, structural, and magnetocaloric effects in manganites (specifically $La_{1-x}A_xMnO_3$) is closely linked to factors such as grain size and surface morphology. Enhanced physical characteristics result from raising the sintering temperature, promoting grain enlargement, and facilitating the development of a more robust microstructure [20]. Baaziz et. al. investigated the impact of grain size and sintering temperature on the critical behavior near the phase transition temperature from paramagnetic to ferromagnetic states in $La_{0.67}Sr_{0.33}MnO_3$ nanoparticles [21]. They concluded that grain size variations play a significant role in determining the universal characteristics of the material in this transition. The variation in temperature and sintering time (600°C, 5 hours and 900°C, 24 hours) on the $(La_{1-x}Ag_x)_{0.8}Ca_{0.2}MnO_3$ material, which was researched by Kurniawan et.al., shows that the longer duration and higher temperature of sintering make the nucleation process in the sample better [22]. Microstructural investigations revealed that the average grain size of LSMO increased due to enhanced grain growth at higher sintering temperatures [1], [3], [7].

$La_{1-x}A_xMnO_3$ is a modified material derived from the parent compound $LaMnO_3$ which has a perovskite structure with a rhombohedral crystal structure. Substituting atoms at the A-site can lead to distortions in the crystal structure, resulting in different physical properties compared to the parent or undoped compounds. The impact of partial substitution on the crystal structure can range from changes in lattice parameters to alterations in the overall crystal structure depending on the doping level [23], [24].

In this study, the impact of sintering temperature on the phase characteristics and grain size of $La_{0.7}AE_{0.3}MnO_3$ (AE=Ba/Ca/Sr) material synthesized by the sol-gel method was investigated. The grain size was controlled by varying the sintering temperature at 700˚C, 800˚C, 900˚C, and 1200˚C, respectively. Characterization was carried out using X-ray Diffraction (XRD) and Scanning Electron Microscope (SEM) to analyze the influence of different sintering temperatures on the material.

The XRD analysis was employed to determine the phase composition and crystal structure of the synthesized $La_{0.7}AE_{0.3}MnO_3$ (AE=Ba/Ca/Sr) material at each sintering temperature. Changes in the diffraction patterns and peak positions were examined to understand the structural evolution with temperature variation. SEM imaging was utilized to observe the morphology and grain size of the $La_{0.7}AE_{0.3}MnO_3$ (AE=Ba/Ca/Sr) samples sintered at different sintering temperatures. The images captured at various magnifications provided insight into the microstructure and grain growth as a function of sintering temperature.

Overall, this comprehensive analysis aimed to elucidate the relationship between sintering conditions, phase formation, and microstructural characteristics in $La_{0.7}AE_{0.3}MnO_3$ (AE=Ba/Ca/Sr) compounds synthesized by the sol-gel method.

2. Experimental Materials and Instruments

The material $La_{0.7}AE_{0.3}MnO_3$ (AE=Ba/Ca/Sr) was synthesized using the sol-gel method. The stoichiometric proportions used were La_2O_3 (Merck, 99%), $Ba(NO_3)_2$ (Merck, 99%), $Ca(NO_3)_2$.$4H_2O$ (Merck, 99%), $Sr(NO_3)_2$ (Merck, 99%), $Mn(NO_3)_2$.$4H_2O$ (Merck, 98.5%), and $C_6H_8O_7$.H_2O (Merck, 99.5%) which were weighed according to their respective calculation. La_2O_3 was dissolved in nitric acid to obtain a transparent solution. Ba $(NO_3)_2$, $Ca(NO_3)_2$.$4H_2O$, $Sr(NO_3)_2$, $Mn(NO_3)_2$.$4H_2O$, and $C_6H_8O_7$ .H_2O were mixed using aquabides until they were evenly dissolved. All precursors in solution were stirred using a magnetic stirrer and heat was applied to a solution temperature of 70˚C using a magnetic hot plate. An ammonia solution was added to adjust the pH to 7. After reaching a homogeneous condition, the solution was heated to evaporate the excess solvent until the precursor became a gel. The gel was heated at 190˚C in an oven for 2 hours and subjected to combustion. Calcination was performed at a temperature of 600˚C for 6 hours to remove impurities in the form of organic material. Sintering was carried out at temperatures of 700˚C, 800˚C, 900˚C, and 1200˚C for 12 hours on each $La_{0.7}AE_{0.3}MnO_3$ (AE=Ba/Ca/Sr) material.

The $La_{0.7}Ba_{0.3}MnO_3$ (LB), $La_{0.7}Ca_{0.3}MnO_3$ (LC), and $La_{0.7}Sr_{0.3}MnO_3$ (LS) powder samples were characterized at different sintering temperatures of 700˚C, 800˚C, 900˚C, and 1200˚C using X-Ray Diffraction (XRD) analysis. XRD measurements were conducted using an X'pert PANalytical diffractometer equipped with CuKα radiation (λ = 1.5406 Å). The X-ray Diffraction patterns were recorded under consistent operating conditions, covering an angle range between 20° and 90° in 2θ mode with a *step size of* 0.02°. Additionally, the morphology of the $La_{0.7}Sr_{0.3}MnO_3$ material was characterized using a Scanning Electron Microscope (SEM) at different sintering temperatures of 700˚C, 800˚C and 900˚C. The comprehensive characterization approach aimed to investigate the structural evolution and morphology changes of the $La_{0.7}AE_{0.3}MnO_3$ (AE=Ba/Ca/Sr) materials as a function of sintering temperature, providing valuable information on phase formation and microstructural properties.

3. Results and discussion

X-ray diffraction (XRD) at room temperature with CuKα radiation (λ = 1.5406 Å) was employed to determine the structure, phase purity, and homogeneity of $La_{0.7}Ba_{0.3}MnO_3$ (LB), $La_{0.7}Ca_{0.3}MnO_3$ (LC), and $La_{0.7}Sr_{0.3}MnO_3$ (LS) materials. The X-ray Diffraction patterns were recorded under standardized operating conditions, covering an angle range between 20° and 90° with a *step size of* 0.02° in 2θ mode. The diffraction data were processed and analyzed using the Rietveld refinement method implemented in the FullProf program. This analytical approach allowed for detailed characterization of the crystal structure, phase composition, and atomic arrangement within the materials. The observed diffraction peaks were well-matched to the diffraction peaks in Crystallography Open Database (COD) No. 4002490, 1521154, and 1521156 for the LB, LC, and LS

samples, respectively. The results of the diffraction patterns obtained from variations in the doping of LB, LC, and LC materials are depicted in Figures 1-3, showcasing the structural properties and phase behavior associated with these compositions at the atomic scale. The analysis provides valuable insights into the influence of cation doping on the crystallographic features and overall material characteristics of the $La_{0.7}AE_{0.3}MnO_3$ (AE=Ba/Ca/Sr) system.

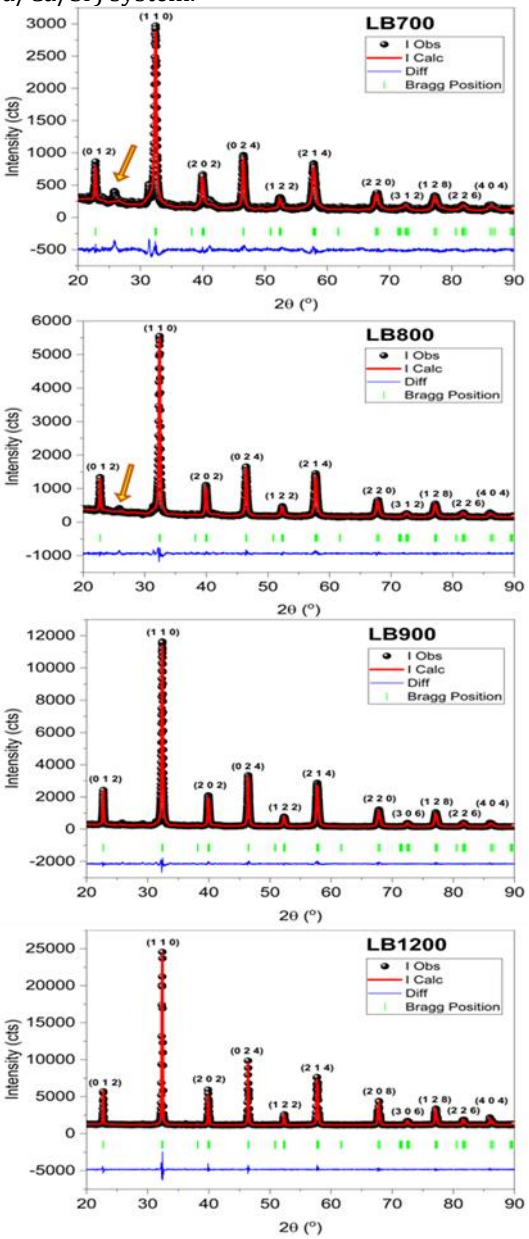

Fig. 1. Diffraction pattern of $La_{0.7}Ba_{0.3}MnO_3$ with variation sintering temperatures of 700˚C, 800˚C, 900˚C, and 1200˚C.

The XRD patterns on LB material with variation sintering temperatures of 800˚C and 900˚C indicate that peaks have been formed in the sample which match the reference which is believed to consist of a single phase. The presence of a low-intensity from $BaMnO_3$ at around the 26.76˚ angle for the 700˚C and 800˚C sintering variations indicates sample contains a secondary phase. The $BaMnO_3$ peak is thought to appear based on the incomplete melting process at temperatures below 800˚C. This matter is assumed based on curve analysis *Thermogravimetric Analysis* (TGA) which has been carried out by Esmaeili, et.al., the TGA curve of LB material shows three area declines that are; (1) At a temperature of 250°C, a significant decrease in sample weight, attribute to the loss of available water, was observed, accounting for more than 50% of the sample. (2) Around 350°, there is likely correlation between nitrate oxidation and changes in composition. (3) Beyond 580°C the synthesis process of LB is completed. Temperatures exceeding 800°C indicate the formation and stabilization of pure perovskite LB nanoparticles [17].

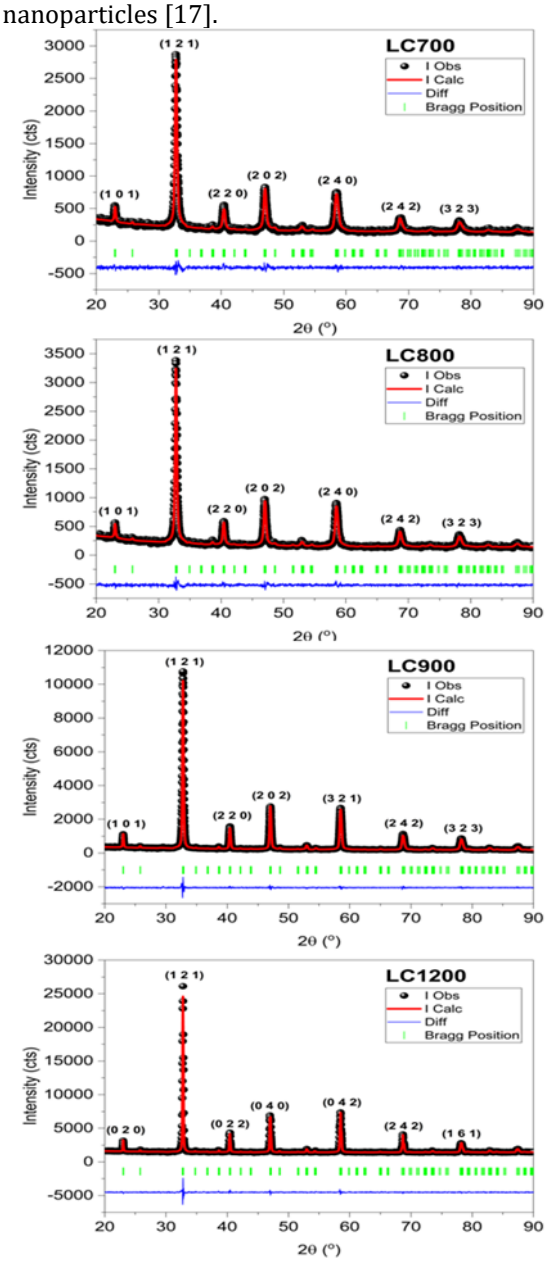

Fig. 2. Diffraction pattern of $La_{0.7}Ca_{0.3}MnO_3$ with variation sintering temperatures of 700˚C, 800˚C, 900˚C, and 1200˚C.

For the LB and LS materials, the most intense peak (110) observed at the sintering temperature of 900°C appeared narrower compared to that at 1200 °C. This narrower peak indicates better crystallinity for the sample sintered at 900°C, suggesting a more ordered and well-defined crystal structure at this temperature [25].

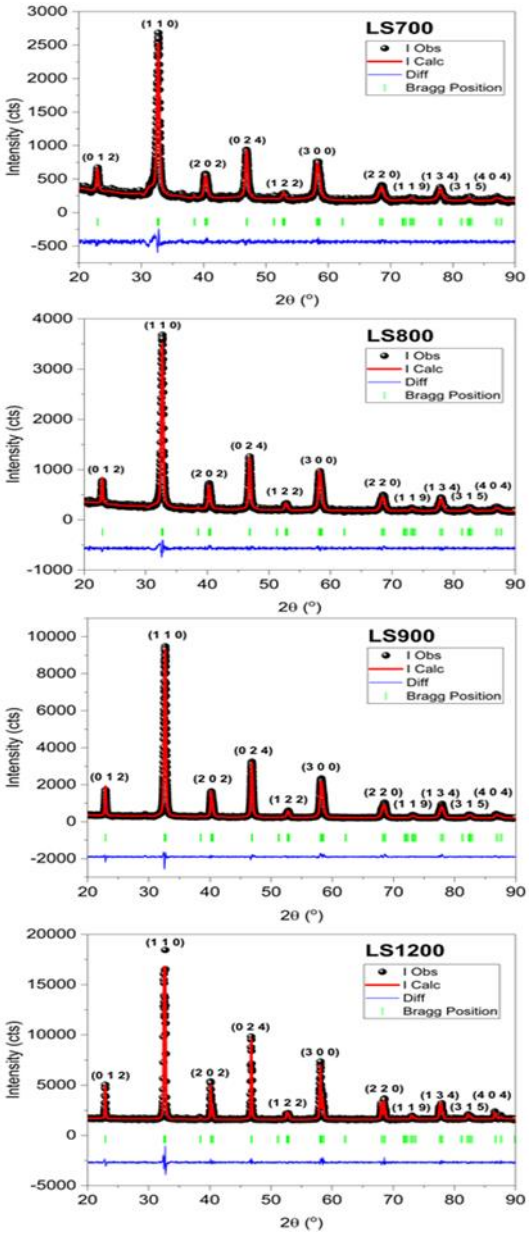

Fig. 3. Diffraction pattern of $La_{0.7}Sr_{0.3}MnO_3$ with variation sintering temperatures of 700°C, 800°C, 900°C, and 1200°C.

In the case of LC and LS materials, the XRD patterns exhibited a single phase for each variation of sintering temperatures, as confirmed by comparison with reference patterns. This observation indicated phase purity and uniformity in the crystallographic structure of these materials under the applied sintering conditions. The single-phase nature of the XRD patterns further supports the suitability of the synthesis method and sintering temperatures for achieving desired material compositions without secondary phases or impurities.

From the diffraction pattern, it can be seen that there is a slight difference in the position of the peaks which is the effect of different sintering temperatures. Based on the Figures 1-3, visible are similarities in LB, LC, and LS, increasing peak intensity and peak shifting ((110) for LB and LS, (121) for LC) in the range of 31°-34° towards higher angles correlated with increased sintering temperature along with a shift value of 2θ, occurs decline Full Width at Half Maximum (FWHM) with increasing sintering temperature. The decline in the FWHM value indicated enhanced crystallinity with increased sintering temperature. The peak shifting in Figure 4 also shows that the unit cell dimensions change and the crystallite size increases with sintering temperature [1], [26]. This shift occurs because the increase in sintering temperature leads to a larger crystallite size due to expansion in lattice parameters [27]. Consequently, the theta value shifted towards lower angle side, this is consistent with Bragg's Law:

$$n\lambda = 2dsin\theta \quad (1)$$

Where n is the diffraction order, λ is the wavelength of the X-Ray, d is the interplanar spacing, and θ is the Bragg angle.

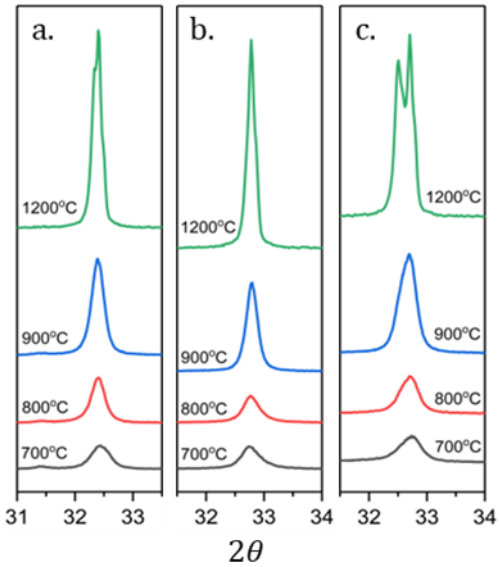

Fig. 4. Peak shifting of a) $La_{0.7}Ba_{0.3}MnO_3$ b) $La_{0.7}Ca_{0.3}MnO_3$, and c) $La_{0.7}Sr_{0.3}MnO_3$ with variation sintering temperatures of 700°C, 800°C, 900°C, and 1200°C.

The suitability of a specific combination of cations to organize into a perovskite structure can be estimated based on the Goldschmidt tolerance factor (t), a dimensionless number, calculated from the ratio of ionic radii. The Goldschmidt tolerance factor ABO_3 compounds are defined as:

$$t = (\langle r_A \rangle + r_o)/\sqrt{2(\langle r_B \rangle + r_o)} \quad (2)$$

Where $\langle r_A \rangle$ is the average ionic radius of cation site A (partly occupied by La and Ba/Ca/Sr), $\langle r_B \rangle$ is the average ionic radius of cation site B (occupied by Mn ions), and r_o is the average ionic radius of the anion. The tolerance factor (t) values are important for predicting structures. Typically, a tolerance factor in the range of 0.8–1.0 is required for the formation of various perovskite structures such as cubic, orthorhombic, or rhombohedral. If $t = 1$, it indicates the formation of an ideal cubic perovskite structure where the size of cation A is slightly larger than that of cation B. Adjusting the ionic radii of the cations relative to the anion can influence the stability and structure of the perovskite material [28]. The results of the Goldschmidt tolerance factor from the calculation for $La_{0.7}Ba_{0.3}MnO_3$, $La_{0.7}Ca_{0.3}MnO_3$, and $La_{0.7}Sr_{0.3}MnO_3$ are 0.971731, 0.940094, and 0.954276, respectively.

Visualization of third variations in doping of the processed material using Visualization for Electronic and Structural Analysis (VESTA) software is shown in Figure 5.

LB and LS indicate rhombohedral symmetry with space group R-3c, whereas LC indicates orthorhombic symmetry with space group Pnma. This result is based on the calculation (2) with the ionic radii for each element specifically Ba = 135pm, Ca = 100pm, and Sr = 118pm which are correlated with the Bravais parameter (a, b, c (Å)) from Rietveld refinement that showed at Table 1. Respectively, for rhombohedral with space group R-3c is a = b ≠ c, α = β = γ ≠ 90° and orthorhombic with space group Pnma is a ≠ b ≠ c, α = β = γ= 90° [29], [30]. The difference in crystal structure, where LB has the same structure as LS but differs from LC, arises from variations in the size of the ionic radii substituting for La (103pm) at site A. Specifically, the ionic radii values for Ba and Sr are bigger than La, while the ionic radius value for Ca is smaller.

The unit cell volume has characteristics in the different phases of the ABO_3 perovskite structure. The unit cell volume per ABO_3 formula unit is defined as $v = {}^{V}/_{z}$, where V is the total volume of the unit cell and z is the number of ABO_3 formula units in each unit cell (z for LB and LS = 6, for LC = 4) [26]. As we can see from Table 1, the unit cell volume of LB, LC, and LS consistently tend to correspond to the ionic radius of the A cation [31], [32]. Compared to Sr^{2+} and Ca^{2+}, Ba^{2+} has the highest unit cell volume which is in line with the largest ionic radii value.

Analysis results from Rietveld refinement for compound $La_{0.7}AE_{0.3}MnO_3$ (AE=Ba/Ca/Sr) show suitability between the appropriate analysis and observed data. Table 1 presents the influence of sintering temperature on the crystallite parameters of the $La_{0.7}AE_{0.3}MnO_3$ (AE=Ba/Ca/Sr) materials after sintering at different temperatures: 700°C, 800°C, 900°C, and 1200°C, as well as the FWHM, the bond length, the bond angles, the average size of the crystallites calculated from the Debye-Scherrer formula and Williamson-Hall, and the disparency factor by Fullprof software.

The variations in these crystallite parameters with sintering temperature provide valuable information on how thermal treatment influences the microstructural properties and crystallographic features of $La_{0.7}AE_{0.3}MnO_3$ (AE=Ba/Ca/Sr) compounds. These detailed analyses contribute to understanding the structure-property relationship and optimizing the synthesis conditions for desired material characteristics.

The increase in cell volume units can indeed be linked to a relationship between lattice parameters and grain size. When the grain size increases, it can lead to an expansion in the lattice due to relaxation strain within the material. This phenomenon is often observed in polycrystalline materials where larger grains contribute to increased cell volumes, reflecting changes in the atomic arrangement and structural integrity of the crystal lattice. Therefore, the enhancement in cell volume units with larger grain sizes suggests the presence of relaxation strain and the influence of grain boundaries on the overall material structure [33]. It has been reported, that lattice strain as inferred from x-ray broadening increases as grain size decreases [34]. The relaxation of strain is linked to an increase in the crystallinity and grain size of the samples. A smaller grain size leads to oxygen vacancies, which disrupt the Mn-O-Mn long-range order or create dislocations at the grain boundaries [35] .

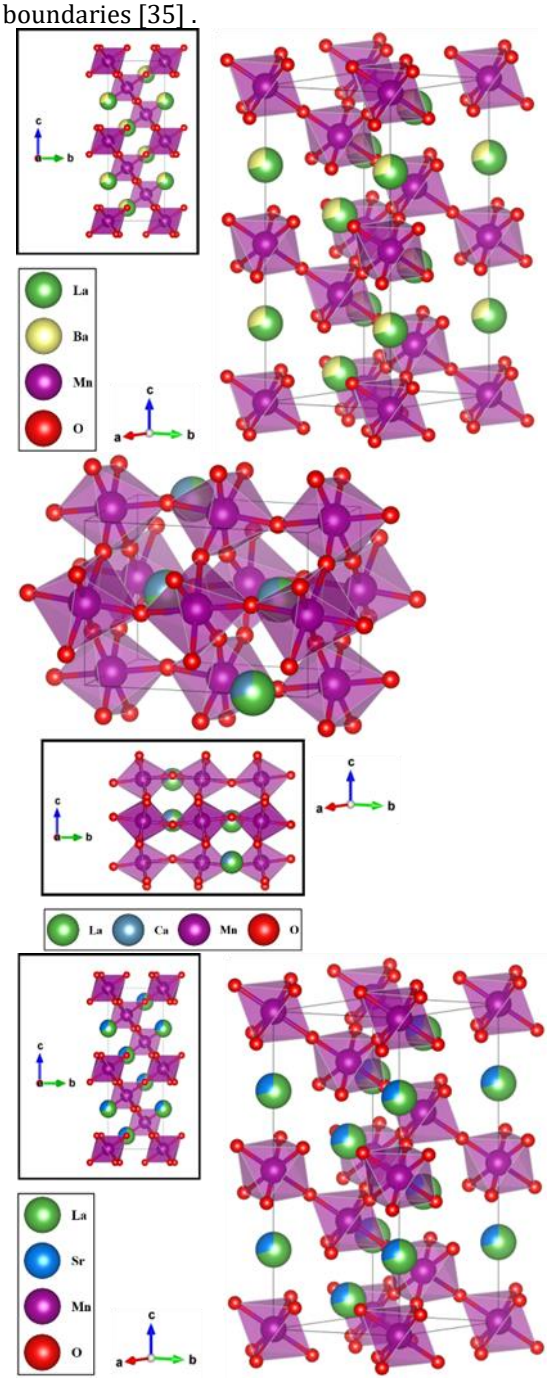

Fig. 5. Visualization of the materials (a) $La_{0.7}Ba_{0.3}MnO_3$ (b) $La_{0.7}Ca_{0.3}MnO_3$, and (c) $La_{0.7}Sr_{0.3}MnO_3$ obtained from VESTA software.

The calculated crystallite size for LB, LC, and LS samples sintered at temperatures of 700°C, 800°C, 900°C, and 1200°C generally increased with higher sintering temperatures. However, for the LS sample, crystallite size decreased at the sintering temperature of 1200°C, this observation correlates with the X-ray diffraction peak analysis, which showed that the sample sintered at 900°C exhibited better crystallinity results. All samples demonstrated reasonably good fits in the XRD analysis, as indicated by the goodness of fit parameter (such as χ^2) derived after refinement, which was found to be less than 3 [25], [36].

The observed decrease in the average bond length ($d_{<Mn-O>}$) with increasing sintering temperature suggests a trend towards shorter Mn-O bond distances. This phenomenon

may be attributed to potential defects in the sub-lattice, which can influence the system's overall stability.

Increasing the sintering temperature likely introduces lattice strain, contributing to changes in the bond lengths within the material [25]. The average bond angle (<Mn-O-Mn>) increases with an increase in the sintering temperature, which is consistent with trends observed in similar systems [1]. These results allow for the confirmation of internal stresses within the structure at different temperatures. Analysis of crystal size and average microstrain for each material was conducted using the Williamson-Hall method, expressed as follows:

$$\beta cos\theta = \frac{k\lambda}{\langle C_{WH} \rangle} + 4\varepsilon sin\theta \quad (3)$$

Where β is the FWHM value of the peak diffraction possessed by the material sample, λ indicates long wave CuKα (1.5406Å), C_(W-H) is the size of the average crystallites possessed by the sample, ε is the strain microstructure owned by the sample, and θ is the corner place peak diffraction as the basis of the FWHM measurement [37].

Table 1. Structural parameters $La_{0.7}AE_{0.3}MnO_3$ (AE=Ba/Ca/Sr) at different sintering temperatures obtained from Rietveld refinement of XRD analysis.

Sample	a (Å)	b (Å)	c (Å)	V (Å³)	Z	v (Å³)	d $_{<Mn-O>}$ (Å)	<Mn-O-Mn> (θ)	$< C_S >$ (nm)	$< C_{W-H} >$ (nm)	ε(%)	R_P (%)	R_{WP} (%)	GoF (χ^2)
LB 700	5.5307	5.5307	13.466	356.722	6	59.45	1.95806	170.6095	23	54	0.19	24.4	22.4	1.95
LB 800	5.5342	5.5342	13.5016	358.122	6	59.69	1.96239	169.4207	32	69	0.13	19.6	15.1	1.12
LB 900	5.5351	5.5351	13.5069	358.374	6	59.73	1.96756	166.7827	38	66	0.09	13.4	12.2	1.53
LB 1200	5.536	5.536	13.5076	358.507	6	59.75	1.96388	168.9354	92	111	0.01	11.9	10.5	2.05
LC 700	5.4403	7.749	5.4784	230.952	4	57.74	1.98227	155.5289	25	54	0.21	23.8	18.1	0.89
LC 800	5.4451	7.743	5.4717	230.693	4	57.67	1.94863	166.8151	28	60	0.18	21.7	16.6	0.83
LC 900	5.4516	7.7337	5.4681	230.544	4	57.64	1.96336	159.964	37	72	0.12	15	12	1.12
LC 1200	5.4758	7.717	5.4603	230.730	4	57.68	1.94675	164.6193	77	97	0.02	24.7	12.7	1.65
LS 700	5.4934	5.4934	13.3532	348.976	6	58.16	1.95636	163.9785	20	32	0.14	27.1	19.2	0.97
LS 800	5.4943	5.4943	13.3617	349.315	6	58.22	1.95497	164.8452	24	66	0.22	22.1	15.9	0.88
LS 900	5.4974	5.4974	13.3717	349.973	6	58.33	1.94786	169.1333	29	181	0.24	13.4	11.5	1.32
LS 1200	5.5066	5.5066	13.3666	351.002	6	58.50	1.9542	166.6861	68	97	0.04	22.2	13	2.07

There is a difference in refinement results between Scherrer (C_S) and Williamson-Hall crystallite size (C_{W-H}). This is because the Williamsen-Hall equation reduces to the Scherrer equation when the strain, ε, is set to 0. While Scherrer's equation only considers the effect of crystallite size on peak broadening, the Williamson-Hall equation is better for determining crystallite size because it also takes into account the broadening of its XRD peaks due to stress suitability [26].

In this study, we analyzed one example of a variation, $La_{0.7}Sr_{0.3}MnO$ to confirm that the enhancement of the sintering temperature is in line with the enhancement of the grain size. The morphology of $La_{0.7}Sr_{0.3}MnO_3$ nanoparticles was analyzed using a Scanning Electron Microscope (SEM) Quanta 650, Thermofisher Scientific. Figures 6a, b, and c show representative SEM images of LSMO samples that were sintered at 700˚C (LS 700), 800˚C (LS 800), and 900˚C (LS 900). These pictures show the existing details with various scattered sizes randomly, each showing clear boundaries. By significant, particles this own consistent ball shape with small diameter distribution in size continues to increase with increasing of the sintering temperature.

The specified size with SEM was larger than that specified using Scherrer (C_S) based on the XRD results. The variation in particle size can be attributed to the presence of multiple crystallites within one particle, particularly in polycrystalline samples. This behavior is similar to what has been reported previously [33]. Despite, the discrepancy in particle size concerning sintering temperature exhibits a consistent trend.

The histogram of the grain size distribution of the sintered samples at different variation temperatures shows evidence of grain growth. Image analysis software, ImageJ was utilized to calculate the average diameter of grains in $La_{0.7}Sr_{0.3}MnO_3$ samples, with measured sizes of 41.05nm, 55.07nm, and 69.27nm for LS 700, LS 800, and LS 800, respectively. The movement of grain boundaries is driven by factors proportional to the average curvature at these boundaries, leading to changes in particle volume and subsequent grain growth. Convex grain boundaries of smaller particles tend to move inward, causing the smaller particles to shrink. At higher sintering temperatures, increased thermal energy facilitates grain boundary migration and coalescence, resulting in larger grain sizes and a broader distribution of grain sizes within the material. Therefore, the observed increase in grain size with higher sintering temperatures is attributed to enhanced grain boundary mobility and coalescence, driven by thermal energy, leading to significant changes in microstructure and grain size distribution in the $La_{0.7}Sr_{0.3}MnO_3$ material [38].

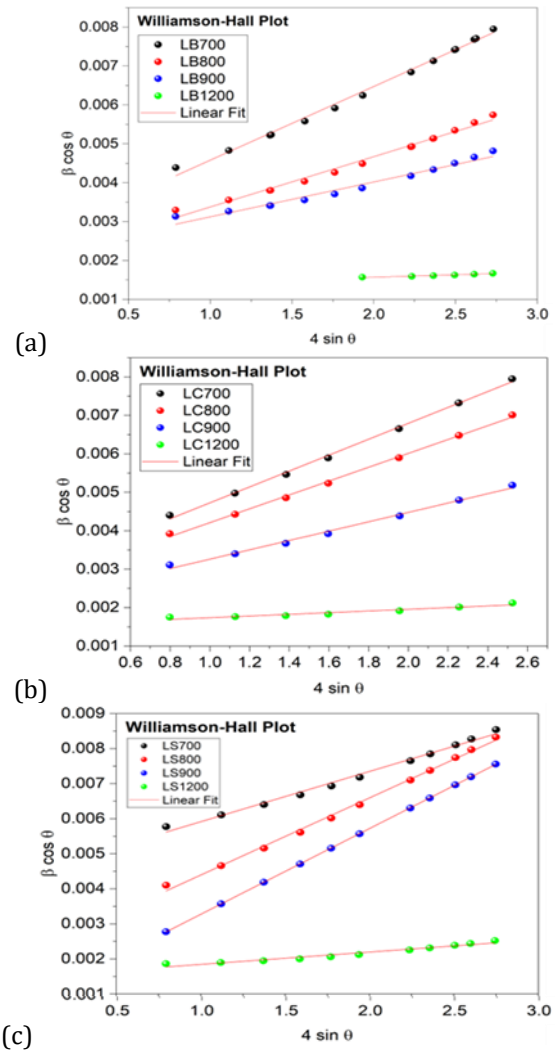

Fig. 6. Williamson-Hall plot against the existence of crystals (a) $La_{0.7}Ba_{0.3}MnO_3$ (b) $La_{0.7}Ca_{0.3}MnO_3$ and (c) $La_{0.7}Sr_{0.3}MnO_3$.

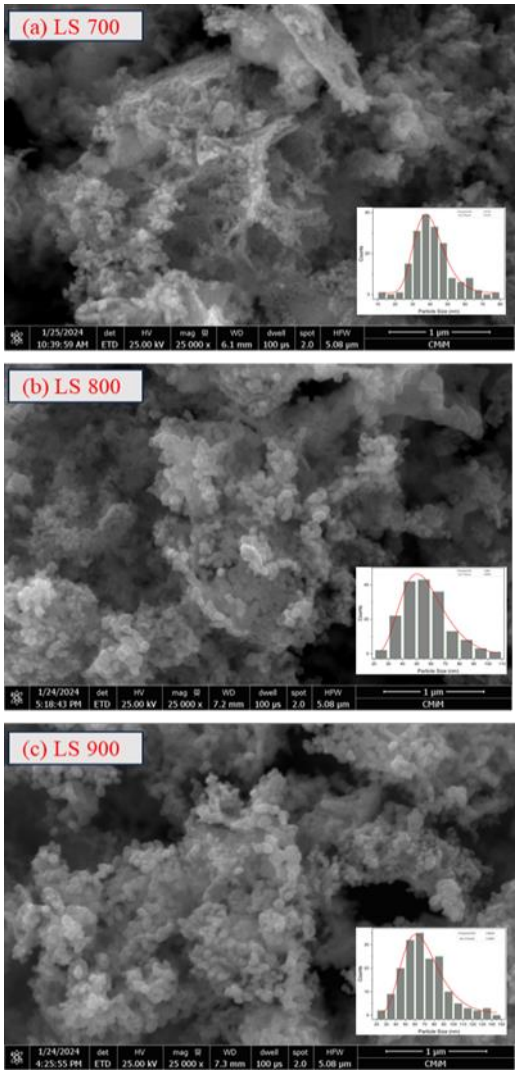

Fig. 7. SEM images of the $La_{0.7}Sr_{0.3}MnO_3$ material with variation sintering temperature at (a) 700˚C (b) 800˚C, and (c) 900˚C.

4. Conclusions

In this study, the impact of sintering at different temperatures on the grain size of $La_{0.7}AE_{0.3}MnO_3$ (AE=Ba/Ca/Sr) prepared by sol-gel method was investigated. X-ray diffraction (XRD) analysis revealed that the LB and LS materials crystallized in rhombohedral symmetry with space group R-3c, while the LC material exhibited orthorhombic symmetry with space group Pnma. The refinement of the X-ray diffraction pattern indicated that a sintering temperature above 800˚C was optimal for the LB sample, as lower temperatures led to the presence of impurities in the XRD pattern. Additionally, slight shifts in peak positions were observed across all samples, indicating the influence of sintering temperature on crystal structure. Scanning Electron Microscope (SEM) analysis provided insights into the morphology of LS samples sintered at different temperatures, showing an increase in particle size with higher sintering temperatures. Both XRD and SEM analyses confirmed the increase in crystallite size and grain size with increasing sintering temperature which led to controlling the structural and morphological properties of La0.7AE0.3MnO3 (AE=Ba/Ca/Sr) compounds.

Acknowledgements

I would like to express my gratitude to the Indonesia Endowment Fund for Education (LPDP) from the Ministry of Finance Republic of Indonesia for providing a scholarship and supporting this research. This work was partially funded by the Directorate of Research and Development, University of Indonesia with contract No. NKB-970/UN2.RST/HKP.05.00/2022.

Conflicts of Interest

The author declares that there is no conflict of interest regarding the publication of this article.

References

[1] Hizi, W., Rahmouni, H., Gorji, N.E., Guesmi, A., Ben Hamadi, N., Khezami, L., Dhahri, E., Khirouni, K. and Gassoumi, M., 2022. Impact of sintering temperature on

the electrical properties of $La_{0.9}Sr_{0.1}MnO_3$ manganite. *Catalysts*, *12*(3), p.340.

[2] Rina, K., Muzakkiy, P.M.A., Engkir, S., Herry, M. and Iwan, S., 2021, November. Neutron diffraction study on nuclear and magnetic structure of (1-x) $La_{0.8}Ba_{0.2}MnO_3$/(x)$Bi_{0.5}Na_{0.5}TiO_3$ composite. In *AIP Conference Proceedings* (Vol. 2381, No. 1). AIP Publishing.

[3] Kekade, S.S., Yadav, P.A., Thombare, B.R., Dusane, P.R., Phase, D.M., Choudhari, R.J. and Patil, S.I., 2019. Effect of sintering temperature on electronic properties of nanocrystalline $La_{0.7}Sr_{0.3}MnO_3$. *Materials Research Express*, *6*(9), p.096108.

[4] Li, S.B., Wang, C.B., Liu, H.X., Li, L., Shen, Q., Hu, M.Z. and Zhang, L.M., 2018. Effect of sintering temperature on structural, magnetic and electrical transport properties of $La_{0.67}Ca_{0.33}MnO_3$ ceramics prepared by Plasma Activated Sintering. *Materials Research Bulletin*, *99*, pp.73-78.

[5] Li, J., Wang, H., Liang, Z., Li, Y., Chen, Q., Zhang, H. and Li, Y., 2022. Improvement of electrical and magnetic properties in $La_{0.67}Ca_{0.33}Mn_{0.97}Co_{0.03}O_3$ ceramic by Ag doping. *Ceramics International*, *48*(24), pp.36888-36899.

[6] Hwang, H.Y., Cheong, S.W., Radaelli, P.G., Marezio, M. and Batlogg, B., 1995. Lattice Effects on the Magnetoresistance in Doped $LaMnO_3$. *Physical review letters*, *75*(5), p.914.

[7] Pan, K.Y., Shaari, A.H., Chen, S.K., Pah, L.K., Navasery, M. and Kechik, M.M.A., 2015. Effect of Sintering Temperature on Structural, Electrical and Magnetic Properties of $La_{0.7}Sr_{0.3}MnO_3$. *Advanced Materials Research*, *1107*, pp.283-288.

[8] Mu, Z., Wei, G., Zhang, H., Gao, L., Zhao, Y., Tang, S. and Ji, G., 2022. The dielectric behavior and efficient microwave absorption of doped nanoscale $LaMnO_3$ at elevated temperature. *Nano Research*, *15*(8), pp.7731-7741.

[9] Urquizo, I.F., Correa, H.S., de Oca Ayala, F.M., de la Rosa, J.R. and García, T.H., 2020. Synthesis of La–Sr–Mn–O and La–Sr–Ca–Mn–O perovskites through solution combustion using urea at fuel deficient conditions. *IEEE Transactions on NanoBioscience*, *19*(2), pp.183-191.

[10] Kharrat, N., Chihaoui, S., Cheikhrouhou-Koubaa, W., Koubaa, M. and Cheikhrouhou, A., 2018. Structural, magnetic and magnetocaloric investigation of La 0.67 Ba0.33$Mn_{1-x}Ni_xO_3$ (x= 0,0.025 and 0.075) manganite. *Journal of Materials Science: Materials in Electronics*, *29*, pp.17187-17194.

[11] Lee, S., Kim, M., Lee, K.T., Irvine, J.T. and Shin, T.H., 2021. CO2 Electrolysis Cells: Enhancing Electrochemical CO2 Reduction using Ce (Mn, Fe) O2 with La(Sr)Cr(Mn)O_3 Cathode for High-Temperature Solid Oxide Electrolysis Cells (Adv. Energy Mater. 24/2021). *Advanced Energy Materials*, *11*(24), p.2170089.

[12] Zhongming, Z., Linong, L., Xiaona, Y., Wangqiang, Z. and Wei, L., 2021. A-site defects in $LaSrMnO_3$ perovskite-based catalyst promoting NO_x storage and reduction for lean-burn exhausts.

[13] Jayakumar, G., Poomagal, D.S., Albert Irudayaraj, A., Dhayal Raj, A., Kethrin Thresa, S. and Akshadha, P., 2020. Study on structural, magnetic and electrical properties of perovskite lanthanum strontium manganite nanoparticles. *Journal of Materials Science: Materials in Electronics*, *31*(23), pp.20945-20953.

[14] Rajan, S., Kumar, A.K. and Isac, J., 2021. Colossal magnetoresistance of Nd-doped $LaCaMnO_3$ polycrystalline ceramics. *Processing and Application of Ceramics*, *15*(1), pp.95-99.

[15] Felhi, H., Brahem, R.A., Smari, M., Skini, R., Alamri, M.A., Selmi, M. and Dhahri, E., 2024. The Impact of Involving Silver into $LaCaMnO_3$ Perovskite on the Magnetocaloric Effect and Electrical Behavior. *Journal of Low Temperature Physics*, *214*(5), pp.281-293.

[16] Rajan, S. and Isac, J., 2021, July. A study on magnetic and spin polarized electric transport properties of cation doped LaCaMnO3perovskite ceramic system. In *IOP Conference Series: Materials Science and Engineering* (Vol. 1166, No. 1, p. 012005). IOP Publishing.

[17] Esmaeili, S., Ehsani, M.H. and Fazli, M., 2020. Photo-catalytic activities of $La_{0.7}Ba_{0.3}MnO_3$ nanoparticles. *Optik*, *216*, p.164812.

[18] Chand, U., Yadav, K., Gaur, A. and Varma, G.D., 2010. Effect of different synthesis techniques on structural, magnetic and magneto-transport properties of $Pr_{0.7}Sr_{0.3}MnO_3$ manganite. *Journal of Rare Earths*, *28*(5), pp.760-764.

[19] Navas, D., Fuentes, S., Castro-Alvarez, A. and Chavez-Angel, E., 2021. Review on sol-gel synthesis of perovskite and oxide nanomaterials. *Gels*, *7*(4), p.275.

[20] Tokkaya, A., Çetin, S.K., Altan, B., Coşkun, A., Taşarkuyu, E. and Ekicibil, A., 2022. Effect of Sintering Time on the Crystallisation, Morphology, Structure, Electric, Magnetic and Magnetocaloric Properties of $La_{0.80}Ag_{0.20}MnO_3$. *Journal of Superconductivity and Novel Magnetism*, pp.1-12.

[21] Baaziz, H., Tozri, A., Dhahri, E. and Hlil, E.K., 2018. Influence of grain size and sintering temperature grain size on the critical behavior near the paramagnetic to ferromagnetic phase transition temperature in $La_{0.67}Sr_{0.33}MnO_3$ nanoparticles. *Journal of Magnetism and Magnetic Materials*, *449*, pp.207-213.

[22] Kurniawan, B., Rosanti, S.D., Kamila, R., Sahara, N.B., Razaq, D.S., Komala, T. and Munazat, D.R., 2018, May. Effect of Temperature and Duration of Sintering on Perovskite Material $(La_{1-x}Ag_x)_{0.8}Ca_{0.2}MnO_3$. In *IOP Conference Series: Materials Science and Engineering* (Vol. 367, No. 1, p. 012055). IOP Publishing.

[23] Ding, S., Li, Y., Guo, J., Wu, D., Wang, S., Deng, X., Xie, Y., Chen, Q. and Zhang, H., Effect of Sm3+ Doping on Tcr and

Mr Properties of $La_{0.7}ca_{0.3}mno_3$ Ceramics. *Available at SSRN 4820631*.

[24] Razaq, D.S. and Kurniawan, B., 2019, March. Preparation and crystal structure of $La_{0.7}Ba_{0.1}Sr0.2Mn_{0.9}Cu_{0.1}O_3$ perovskite: a comparison between sol-gel and solid state process. In *Journal of Physics: Conference Series* (Vol. 1170, No. 1, p. 012050). IOP Publishing.

[25] Mesrar, M., Lamcharfi, T., Echatoui, N.S. and Abdi, F., 2022. Effect of sintering temperature on the microstructure and electrical properties of $(Na_{0.5}Bi_{0.5})TiO_3$ processed by the sol-gel method. *Journal of Sol-Gel Science and Technology*, *103*(3), pp.820-831.

[26] Khoshnood, R.S. and Khoshnoud, D.S., 2019. Structural, magnetic, and photocatalytic properties in $Bi_{0.83-x}La_{0.17}Y_xFeO_3$ nanoparticles. *Applied Physics A*, *125*(11), p.750.

[27] Kumar, D., Singh, M. and Singh, A.K., 2018, May. Crystallite size effect on lattice strain and crystal structure of $Ba_1/4Sr_3/4MnO_3$ layered perovskite manganite. In *AIP Conference Proceedings* (Vol. 1953, No. 1). AIP Publishing.

[28] Kour, R., Arya, S., Verma, S., Gupta, J., Bandhoria, P., Bharti, V., Datt, R. and Gupta, V., 2019. Potential substitutes for replacement of lead in perovskite solar cells: a review. *Global Challenges*, *3*(11), p.1900050.

[29] Silva-Ramírez, E.L., Cumbrera-Conde, I., Cano-Crespo, R. and Cumbrera, F.L., 2023. Machine learning techniques for the ab initio Bravais lattice determination. *Expert Systems*, *40*(2), p.e13160.

[30] Simons, H., Daniels, J., Jo, W., Dittmer, R., Studer, A., Avdeev, M., Rödel, J. and Hoffman, M., 2011. Electric-field-induced strain mechanisms in lead-free $94\%(Bi_{1/2}Na_{1/2})TiO_3-6\%BaTiO_3$. *Applied Physics Letters*, *98*(8).

[31] Denisenko, Y.G., Molokeev, M.S., Oreshonkov, A.S., Krylov, A.S., Aleksandrovsky, A.S., Azarapin, N.O., Andreev, O.V., Razumkova, I.A. and Atuchin, V.V., 2021. Crystal structure, vibrational, spectroscopic and thermochemical properties of double sulfate crystalline hydrate $[CsEu(H_2O)_3(SO_4)_2]\cdot H_2O$ and its thermal dehydration product $CsEu(SO_4)_2$. *Crystals*, *11*(9), p.1027.

[32] Kim, S.J., Demazeau, G., Alonso, J.A. and Choy, J.H., 2001. High pressure synthesis and crystal structure of a new Ni (III) perovskite: $TlNiO_3$. *Journal of Materials Chemistry*, *11*(2), pp.487-492.

[33] Yadav, P.A., Deshmukh, A.V., Adhi, K.P., Kale, B.B., Basavaih, N. and Patil, S.I., 2013. Role of grain size on the magnetic properties of $La_{0.7}Sr_{0.3}MnO_3$. *Journal of magnetism and magnetic materials*, *328*, pp.86-90.

[34] Mohamed, F.A., 2019. Correlation between the minimum grain size obtainable by ball milling and lattice strain. *Materials Science and Engineering: A*, *752*, pp.15-17.

[35] Ng, S.W., Lim, K.P., Halim, S.A. and Jumiah, H., 2018. Grain size effect on the electrical and magneto-transport properties of nanosized $Pr_{0.67}Sr_{0.33}MnO_3$. *Results in Physics*, *9*, pp.1192-1200.

[36] Bhattacharyya, R., Das, S., Das, A. and Omar, S., 2021. Effect of sintering temperature on the microstructure and conductivity of $Na_{0.54}Bi_{0.46}Ti_{0.99}Mg_{0.01}O_{3-\delta}$. *Solid State Ionics*, *360*, p.115547.

[37] Kurniawan, B., 2024. Identifikasi Fasa dan Informasi Kristal Nanopartikel Oksida Spinel $CuCr_2O_4$ Memanfaatkan Analisis XRD Berbasis Metode Rietveld Refinement. *JIIF (Jurnal Ilmu dan Inovasi Fisika)*, *8*(1), pp.9-16.

[38] Lee, J., Jeong, J., Lee, H., Park, J., Jang, J. and Jeong, H., 2023. Effects of Sintering Processes on Microstructure Evolution, Crystallite, and Grain Growth of MoO_2 Powder. *Crystals*, *13*(9), p.1311.